https://doi.org/10.5194/egusphere-2025-5317
Preprint. Discussion started: 16 December 2025


# GHOST aurora - continuum emission produced by hot $N_2$

Rowan Dayton-Oxland[1], Fiona Ball[1], Daniel Whiter[1], Srimoyee Samaddar[1], Noora Partamies[2], Mathieu Barthelemy[3], Katie Herlingshaw[2], and Eero Karvinen[4]

[1]University of Southampton, University Road, Southampton, SO17 1BJ, United Kingdom
[2]University Centre in Svalbard, Longyearbyen, Svalbard
[3]Univ. Grenoble Alpes, CNRS, IPAG, 38000 Grenoble, France
[4]Citizen scientist

**Correspondence:** Rowan Dayton-Oxland (R.A.Dayton-Oxland@soton.ac.uk)

**Abstract.** We investigate the origin of the continuum emissions observed in the poleward boundary dayside aurora discovered in Partamies et al. (2025), known as GHOST, and propose that they arise from highly excited, hot $N_2$. Using spectral modelling and fits to ground-based measurements of high-resolution GHOST spectra, we demonstrate that vibrationally and rotationally excited $N_2$ and $N_2^+$ can reproduce the observed structured continuum without requiring emission from NO. Spectral fitting indicates that GHOST events coincide with extreme ion heating and high neutral temperatures. Background conditions from additional events indicate that strong ionospheric flows are typically present, which can help to provide the necessary energy input for producing hot neutral and ionised $N_2$. Proton aurora observations and EISCAT incoherent scatter radar measurements of ionospheric plasma parameters indicate that two of our three events are located in the cusp. These results suggest that the combination of strong flow, heating, particle precipitation, and cusp conditions produce thermally excited $N_2$ populations which can account for the continuum spectrum of GHOST.

## 1 Introduction

While atmospheric continuum emissions have been known to the field of airglow for decades (Meinel, 1953; Sternberg and Ingham, 1972; Noll et al., 2024), they had not been observed and studied in aurora and aurora-like emissions until the recent discoveries of STEVE (Strong Thermal Emission Velocity Enhancement; MacDonald et al., 2018), nightside continuum in the aurora (Spanswick et al., 2024; Nanjo et al., 2024), and continuum structures in the poleward boundary of the dayside aurora (Partamies et al., 2025). In this study we call the continuum emission structures within dynamic aurora GHOSTs (backronym-ed as Geo-magnetic High-bandwidth Optical Spectra from the Thermosphere) due to their pale, ghostly appearance, and to differentiate the particle precipitation related continuum from the plasma flow driven continuum, like STEVE. To be exact, continuum should only refer to a true continuum spectrum, like that produced by thermal blackbody radiation or Bremsstrahlung, a completely non-discrete mechanism. However, other studies in the airglow and aurora fields have referred to molecular pseudo-continuum as 'continuum', or used both interchangeably. All mentions of continuum here are addressing molecular pseudo-continuum.

https://doi.org/10.5194/egusphere-2025-5317
Preprint. Discussion started: 16 December 2025


Similar spectral properties and visually similar emission to STEVE observations were found within the dayside aurora over Svalbard, Arctic Norway by Partamies et al. (2025). They described two dayside auroral events where the dayside red emission was accompanied by white or pale pink continuum emission. These emission structures lasted for tens of minutes but unlike the STEVE continuum, they followed the dynamics and the evolution of auroral structures. Spectral evidence from a co-located spectrograph was presented for the two dayside events, showing a pseudo-continuum emission. In addition, similarly coloured emission structures were reported in the afternoon and nightside aurora without simultaneously measured spectra. Along with the optical observations, the dayside continuum emissions presented by Partamies et al. (2025) were observed by the EISCAT incoherent scatter radar, Fabry-Perot Interferometer and an overpassing Defence Meteorological Satellite Program (DMSP) satellite. They provided evidence on enhanced plasma and neutral gas heating and upwelling, as well as a strong horizontal shear flow across the emission structure for one of the events. These parameters were deemed comparable to the heating and shear flow observed in connection with STEVE.

Independently, continuum emission was found within the dynamic nightside aurora over Rabbit Lake in Canada (Spanswick et al., 2024). This study reported 30 continuum emission events captured by the Canadian Transition Region Explorer (TREx) RGB all-sky camera and meridian imaging spectrograph. The continuum emission conditions were quantified to be at least about 20 R/nm brightness level across the visible wavelength range. An integrated luminosity at 502–507 nm was used as an indicator for continuum emission, as it is a wavelength region where the ionosphere does not include strong auroral or airglow emission lines. The sizes of these emission structures ranged from 20 to 500 km with lifetimes of minutes and less. Compared to the dayside events, the nightside continuum emission structures appeared more white/gray (or less pink) and more transient.

The cusp is a region of the dayside ionosphere where there is direct solar wind precipitation along field lines opened by reconnection. The cusp can be identified by the ionospheric footprints of flux transfer events (a type of energetic pulsed reconnection occurring at the magnetopause) (Goertz et al., 1985) which produce visual poleward moving auroral forms (Sandholt et al., 1986, 1992), pulsed ionospheric flows in radar(Pinnock et al., 1993), and pulsed proton events Moen et al. (1998); Deehr and Lummerzheim (2001) in proton aurora measurements.

The largest continuum emission structures in Partamies et al. (2025) occurred within dayside aurora in sunlit ionosphere with shadow heights around 160 km. The auroral emission in those conditions is predominantly red with a purple hue from the molecular nitrogen emission. Dayside blue emission is primarily due to resonance scattering, in which upwelling of molecular nitrogen ions into the sunlit heights allows it to absorb and emit at its characteristic blue light at 428 $\mathrm{nm}$ (Shiokawa et al., 2019).

STEVE is driven primarily by Subauroral Ion Drift (SAID) events (MacDonald et al., 2018), with extreme ion drift velocity and electron temperature in the highest 5% and 3% compared with non-STEVE SAID events, corresponding to about 3 km/s and 4000–10000 K (Archer et al., 2019). Similarly in GHOSTs, Partamies et al. (2025) reported high cross-track shear velocity of 4 km/s in each direction measured by the DMSP satellite, and high ion (2500–3000 K) and electron (3000–4000 K) temperatures measured by EISCAT Svalbard radar.

Spectral studies of STEVE show an enhanced emission brightness across the entire optical range and slightly into the infrared. Gillies et al. (2019) presented TREx spectrograph data of a STEVE showing elevated continuum emission from 400–

https://doi.org/10.5194/egusphere-2025-5317
Preprint. Discussion started: 16 December 2025


800 nm, supported by Liang et al. (2019). Even with the strongest auroral emission lines at 428, 558 and 630 nm subtracted, the total brightness of the continuum emission across the wavelength range gave twice as high values as the background sky.

Airglow continuum emissions have long been attributed to the nitric oxide mechanism $NO + O \rightarrow NO_2 + h\nu$ (e.g. Meinel, 1953). This same mechanism has also been considered for STEVE, initially suggested by Gillies et al. (2019), further developed by Harding et al. (2020), Mende et al. (2019), Mishin and Streltsov (2022), and Nanjo et al. (2024), and recently disputed by Liang and Donovan (2024). The NO continuum mechanism was also discussed as a potential mechanism for GHOST emission (Partamies et al., 2025), who presented high-resolution (sub-Ångström resolution) spectra evidencing the continuum's molecular structure for the first time. Spanswick et al. (2024) also considered NO to explain their observed continuum, which they used to rule out FeO and NiO as potential emitting species. They further presented a comparison of the continuum emission brightness with expected $NO_2$ brightness at discrete points. In conclusion they suggested that the $N_2$ 1P (first positive), 2P (second positive) and $N_2^+$ 1N (first negative) bands may be embedded in the continuum spectrum.

All the previous studies have focused on the NO reaction because it does produce a pseudo-continuum emission i.e. broadband emission which appears close to a true continuum, but contains discrete structure, indicating it is composed of many densely packed emission lines. However, the production of sufficient NO for the observed continuum brightness leads to challenges. In the case of STEVE, Harding et al. (2020) presented two NO production pathways;

$$N_2[A^3\Sigma_u^+] + O \rightarrow NO + N(^2D) \tag{R1}$$

$$N_2[X^1\Sigma_g^+(v > 11)] + O \rightarrow NO + N \tag{R2}$$

where v is the quantum vibrational number. Reaction R1 requires $N_2$ in the Vegard-Kaplan band system upper state, requiring energies $> 6$ eV, while Reaction R2 requires $N_2$ with vibrational level higher than 11, which has a lower energy requirement of 3 eV, and so was considered more likely.

Liang and Donovan (2024) calculated the vibrational excitation of $N_2$ molecules by collision with drifting ions, specifically the vibrational-translational energy transfer. Under typical SAID conditions, the resulting density of $N_2^*$ was found to be too low to produce enough NO to explain the observed STEVE brightness. Within the airglow community, the NO mechanism has been questioned by several authors (e.g. Bates, 1993; Evans et al., 2010), who have pointed out discrepancies between the proposed chemistry and the observed spectra, suggesting that the observed spectrum results from metastable oxygen and FeO respectively.

NO requires high energy to produce and is strongly reactive. The problems with the NO mechanism suggest that an alternative continuum-producing mechanism is possible. In this work we will argue that sufficiently heated $N_2$ itself is capable of producing (pseudo-)continuum emissions which explain the observed spectra well.

https://doi.org/10.5194/egusphere-2025-5317
Preprint. Discussion started: 16 December 2025


## 2 Instrumentation and data

We use full-colour all-sky camera (ASC) data from Kjell Henriksen Observatory (KHO, 78.25°N, 16.04°E, Herlingshaw et al. (2024)) on Svalbard in arctic Norway for identifying GHOST events. This ASC is a Sony $\alpha$7s mirrorless DSLR, which has been in operation since late 2015. The raw data has a pixel resolution of 2832×2832. Nighttime images with 4-second exposure time have been taken at a cadence of 12 seconds throughout the winter seasons, which on Svalbard extend from the beginning of November until the end of February. Images are captured when the Sun is below the horizon. The continuum emission in these images looks white, pale pink or orange, none of which matches the normal auroral emissions of green, red and blue light. For context, an animation of GHOST evolution was provided in the supplementary material of Partamies et al. (2025).

We acknowledge that white or grey colour in full-colour images can be caused by overlapping green and red emission along the same line-of-sight. We therefore collect spectra from a co-located Meridian Imaging Svalbard Spectrograph (MISS) to confirm our GHOST observations. MISS images a meridian slit (approx. 1 degree wide) to provide spectral information from 400 to 700 nm with a resolution of about 5 nm until late 2024, and 1.5 nm since then. A full spectrum was recorded every minute until late 2024, and every 15 seconds since then.

The High Throughput Imaging Echelle Spectrograph (HiTIES, Chakrabarti et al. 2001) is used to obtain high-resolution spectra of the GHOST emissions. HiTIES is located at the KHO on Svalbard, and is directed at magnetic zenith with a field of view of 8 by 0.05 degrees. The instrument includes an Echelle spectrograph grating, an electron-multiplying charged coupled device (EMCCD) detector, and a mosaic filter which is used to select multiple overlapping spectral orders, enabling observation of multiple non-contiguous wavelength bands at high resolution ($< 0.1$ nm). The mosaic filter selects the H$\alpha$ band at 649–663 $\mathrm{nm}$ used for observing proton precipitation, $O^+$ ($^2$D–$^2$P) emission, hydroxyl airglow OH(8,3) band at 728–743 $\mathrm{nm}$, and OH(5,1) band at 790–807 $\mathrm{nm}$.

The EISCAT Svalbard Radar (ESR, Wannberg et al. 1997) provides ionospheric plasma measurements and is approximately co-located with KHO. We use the ESR run presented by Partamies et al. (2025), but present analysis of the data from the 32m steerable antenna instead of the field-aligned antenna. At the time of the GHOST appearance, the steerable ESR antenna was pointed poleward at an elevation of 30 degrees. We also use Super Dual Auroral Radar Network (SuperDARN, Greenwald et al. 1995) measurements to look at the background global ionospheric convection in the F region and convection cells with respect to the locations of the GHOSTs.

Finally, Interplanetary Magnetic Field (IMF) measurements are taken from the OMNIWeb (King and Papitashvili, 2005), which provides data from multiple satellites propagated to the bow shock.

## 3 Events

### 3.1 Event 1: 3 January 2020, bright large GHOST

The first event studied here is the spectrally confirmed continuum emission event which was seen at the zenith from 08:30 to 09:30 UT on 3 January 2020 (Partamies et al., 2025). Over an extended time interval, GHOST structures were observed to

https://doi.org/10.5194/egusphere-2025-5317
Preprint. Discussion started: 16 December 2025


appear and disappear in the ASC field of view, and temporally and structurally evolve and follow the red emission caused by auroral precipitation in the cusp. During this GHOST evolution, the ionosphere was sunlit above about 160 km, which led the red emission to be accompanied by blue resonance scattering.

### 3.2 Event 2: 28 February 2020, thin isolated GHOST

The second event is an arc-like GHOST identified in ASC images and confirmed by spectral measurements from MISS. This event occurred as an isolated individual continuum structure that persisted about 15 minutes at 03:05-03:20 UT. Figure 1 shows an all-sky view of the event with the GHOST highlighted in the zenith, as well as the MISS spectrogram and pseudo-continuum spectrum. Unlike other high latitude GHOSTs, this structure occurred in vicinity of primarily green aurora and a few hours earlier in the magnetic morning (before cusp) compared to the GHOST Event 1. The spectral measurements of this event show a slightly increasing continuum brightness towards longer wavelengths (bottom left panel in Figure 1). The ionospheric shadow height during this event was about 170 $\mathrm{km}$.

### 3.3 Event 3: 30 December 2021, GHOST conditions

The last event was first identified from the presence of bursty proton aurora and was confirmed by all-sky images and HiTIES spectra. Sparse patches of white GHOST visually appear in ASC images from 09:12 to 09:33 UT against a typical cusp sky, and HiTIES spectra measure sparse, fairly dim continuum from 09:22 to 09:50 UT. None of the GHOST structures were seen in the meridian line for long enough to be captured by MISS. The visual occurrences in the ASC images off the meridian line had the same colour as the GHOSTs seen in Events 1 and 2, as shown by the example images in Figure 2. Based on these images and the HiTIES measurements shown in Figure 3, this event clearly has the correct conditions for GHOST emissions to appear, but it is missing some factor to produce the large GHOST event at the zenith, such as in Event 1.

## 4 Spectral identification

In order to investigate the origin of the continuum spectrum, we fit the observations with model synthetic spectra of various species known to be abundant in the polar atmosphere with emission within our measured spectral range; $N_2$, $N_2^+$, $O_2^+$, and $O^+$ auroral emission and $OH^*$ airglow. We model only the shape of the emission spectrum for each species based on temperature, and do not need to model specific atmospheric conditions since the fit to data leaves the intensities of each molecular vibrational band as free parameters.

Checking the high resolution spectra of $NO_2$ as shown in Smalley et al. (1975) at very low temperatures does not show any specific coincidence when comparing to the H$\alpha$ HITIES spectra shown in Figure 3, or compared with previous high-resolution spectra of GHOST reported in Partamies et al. (2025).

https://doi.org/10.5194/egusphere-2025-5317
Preprint. Discussion started: 16 December 2025


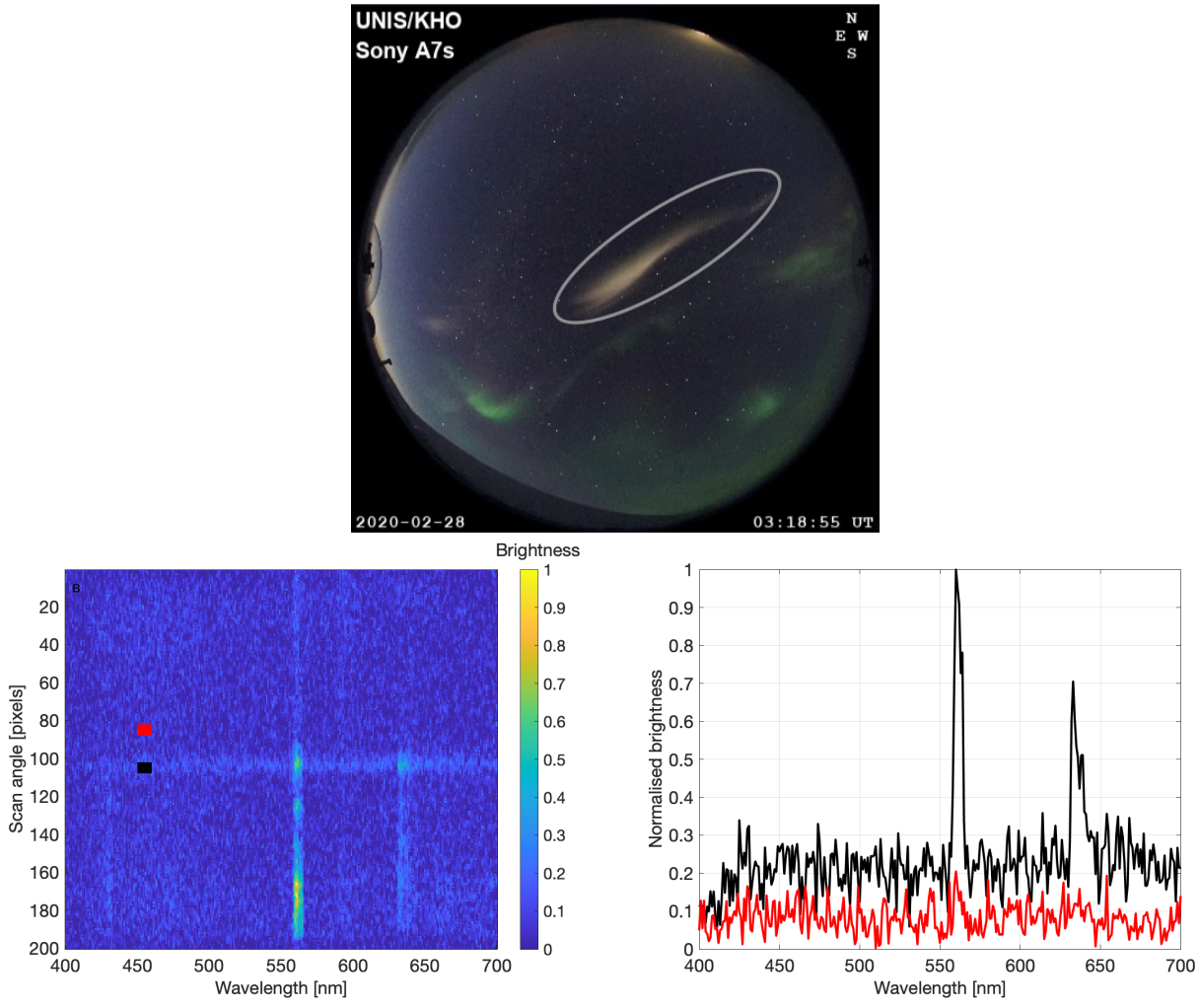


**Figure 1.** Top: GHOST in all-sky image encircled by a gray oval. Bottom left: simultaneous spectrogram along the vertical meridian slice (corresponding to the north-south magnetic meridian) of the image. A zero scan angle corresponds to directly north, 100 to the zenith, and 200 to the south. Bottom right: spectra at the meridian location of the continuum emission (black) as well as an empty sky (red) north of continuum.

### 4.1 Synthetic spectra

The spectral fit uses emissions from excited states of $N_2$ and ionization states of $N_2^+$ and $O_2^+$, containing several key vibrational bands, that emit photons in the optical range. The emissions from excited states of $N_2$ used in this study are the First Positive band system ($N_2$ 1P, decay from the excited electronic $B^3\Pi_g$ state to the $A^3\Sigma_u^+$ state, Naudé 1931), Infra-Red Afterglow (IRA, emission from $B'^3\Sigma_u^-$ to $B^3\Pi_g$, Carroll and Sayers 1953; Carroll and Rubalcava 1959), and Vegard-Kaplan (VK) band system (from the excited $A^3\Sigma_u^+$ state to the ground state $X^1\Sigma_g^+$, Vegard 1930; Kaplan 1934). $N_2^+$ Meinel (M) band emissions from the

https://doi.org/10.5194/egusphere-2025-5317
Preprint. Discussion started: 16 December 2025



**Figure 2.** ASC images of the GHOST structures towards the west horizon during Event 3 taken at 09:15:30, 09:22:50 and 09:24:01 UT. The regions of continuum emission are marked by the gray ovals.

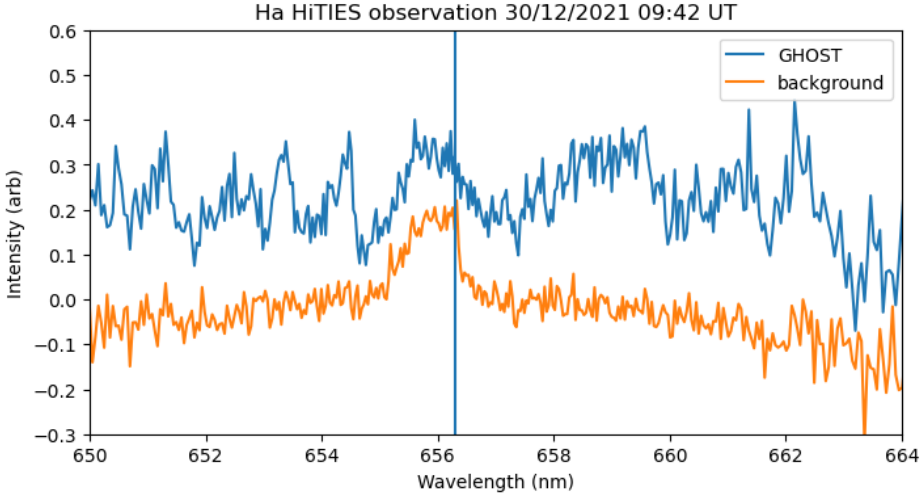


**Figure 3.** Spectrum showing GHOST-like emission (blue) against a background spectrum (orange) in HiTIES on 30/12/2021 taken at 09:42 UT. The H$\alpha$ rest wavelength at 656.3 nm is marked with a blue vertical line, and proton aurora is visible in both the GHOST and background spectra.

$A^2\Pi_u$–$X^2\Sigma_g^+$ transition (Meinel, 1950) and $O_2^+$ First Negative (1N) emissions from the $b^4\Sigma_g^-$–$a^4\Pi_u$ transition (Shemansky and Vallance Jones, 1968) are also included in the synthetic spectra.

155 The total energy of a diatomic molecule is the sum of its electronic ($T_e$), vibrational ($G$) and rotational ($F_v$) energies. The synthetic spectra were constructed after a substantial literature review of the latest available vibrational and rotational constants used to determine the total energies of the five aforementioned emission band systems. For each electronic state, the model

https://doi.org/10.5194/egusphere-2025-5317
Preprint. Discussion started: 16 December 2025


includes 22 vibration levels, and their vibrational, $G(v)$, and rotational, $B(v)$ and $D(v)$, constants are fitted polynomials given by the following standard equations (Laher and Gilmore, 1991). The vibrational energy is obtained from the coefficients of the polynomial fit given by Equation 1:

$$G(v) = w_e\left(v+\frac{1}{2}\right) - w_e x_e\left(v+\frac{1}{2}\right)^2 + w_e y_e\left(v+\frac{1}{2}\right)^3 + w_e z_e\left(v+\frac{1}{2}\right)^4, \quad (1)$$

where $v$ is the vibrational level and all other symbols ($w_e$, $w_e x_e$, $w_e y_e$, $w_e z_e$) are empirically defined constants, primarily obtained from the NIST database (Huber and Herzberg). The other two constants of rotational-vibrational interactions are similarly obtained from Equations 2 and 3:

$$B(v) = B_e - \alpha_e\left(v+\frac{1}{2}\right) + \gamma_e\left(v+\frac{1}{2}\right)^2 \quad (2)$$

$$D(v) = D_e + \beta_e\left(v+\frac{1}{2}\right) + ... \quad (3)$$

,

As for Equation 1, $B_e$, $\alpha_e$, $\gamma_e$, $D_e$, and $\beta_e$ of the polynomial fits in Equations 2 and 3 are primarily obtained from the NIST database (Huber and Herzberg).

The vibrational and rotational constants are then used to obtain the rotational levels for each vibrational band. The rotational energy, $F_v(J)$, for each level $J$ is obtained from the above constants using Equation 4:

$$F_v(J) = B_v J(J+1) - D_v[J(J+1)]^2. \quad (4)$$

The rotational level $J$ is associated with a particular electronic and vibrational motion of the $N_2$ molecule. Emission wavelengths for individual transitions can be obtained from the total energy (electronic + vibrational + rotational), $T_e+G(v)+F_v(J)$.

For each electronic transition, there are several 'branches' (from upper $J'$ to lower $J''$ levels), for example, the ${}^PQ$, ${}^PP$, ${}^RR$ and the ${}^RQ$ branches of the VK band system (Herzberg, 1950; Yonker, 2005), which can be observed in the emission spectra. Theoretically, these rotational branches can be evaluated from quantum mechanical selection rules, which determine which rotational transitions are allowed. We take these selection rules from Schadee (1964), Herzberg (1950) and Tatum (1967), and the model uses these to derive the rotational transitions from the upper to the lower $J$ levels. The rotational branches of the $N_2^+$ Meinel band used in this work are taken from the extensive study of Benesch et al. (1980) and the more recent work by Zhang et al. (2015). The rotational structure of the $N_2$ 1P band system has previously been modelled by Jokiaho (2009) for use with HiTIES observations. The selection rules for the rotational branches of the $N_2$ IRA band system are similar to those of $N_2$ 1P, since both are ${}^3\Sigma - {}^3\Pi$ transitions, and are compiled from work by Herzberg (1950) and Carroll and Rubalcava (1960).

The intensity of each emission line is given by the theoretical relation based on the r-centered approximation (Nicholls and Stewart, 1962; Laher and Gilmore, 1991) as shown in Equation 5:

https://doi.org/10.5194/egusphere-2025-5317
Preprint. Discussion started: 16 December 2025


$$I_{v'v''J'J''} = \frac{64\pi^4\lambda^4 N_{v'}c}{3Q_r}\phi|\mathbf{R_e}(\overline{r}_{v'v''})|^2 q_{v'v''}\zeta_{J'J''}\exp\left\{-\left(F_v(J')+G(v')\right)\frac{hc}{kT}\right\}, \quad (5)$$

where $h$ is Planck's constant, $c$ is the speed of light, $k$ is Boltzmann's constant, and $T$ is the temperature. $F_{v'}(J')$ and $G(v')$ are calculated from Equations 4 and 1, respectively. $Q_r$ is the rotational partition function and is equal to $1+3e^{-2B_v hc/kT}+5e^{-2B_v hc/kT}+...$, but for sufficiently large $T$ or small $B_v$, $Q_r$ can be approximated by $kT/(hcB_v)$ (Herzberg, 1950). The intensity of radiated emission by a population density of $N_{v'}$ in the upper vibrational level $v'$ can be related to the expected value of the electronic transition moment at the r-centroid, $|\mathbf{R_e}(\overline{r}_{v'v''})|$, and the Franck-Condon factor, $q_{v'v''}$, which is the overlap integral, indicating the strength of vibrational transition (Gilmore et al., 1992). These values are obtained from Gilmore et al. (1992), who tabulate the above values for 22 vibrational levels of all five band systems studied here. Similarly, the Hönl-London factors, $\zeta_{J'J''}$, in Equation 5 determine the relative likelihood of the transition from the upper $J'$ to the lower $J''$ rotational branches within a vibrational band of emission. In this study, the Hönl-London factors are obtained from Schadee (1964) and Budó (1937).. Finally, $\phi$ is the statistical weight which is $\frac{2}{3}$ for odd $J'$ and $\frac{1}{3}$ for even $J'$ for $N_2$ (Yonker, 2005).

Wavelengths and relative intensities of OH Meinel (M) system airglow are determined from the data provided by Brooke et al. (2016). The relative intensity of each line within a specific vibrational band is given by:

$$I = A(2J+1)\exp\left(-\frac{hcE}{kT}\right), \quad (6)$$

where $A$ is the Einstein coefficient for the transition, $J$ is the upper state total angular momentum quantum number, $h$ is Plank's constant, $c$ is the speed of light, $E$ is the upper state energy, $k$ is Boltzmann's constant, and $T$ is temperature.

### 4.2 Fit to observations

| Band system | Upper vibrational levels |
|---|---|
| $N_2$ 1P | $v = 4, 5, 6$ |
| $N_2$ IRA | $v = 5, 10, 14, 15, 19$ |
| $N_2$ VK | $v = 0, 1$ |
| $N_2^+$ M | $v = 5$ |
| $O_2^+$ 1N | $v = 0, 1, 2, 3$ |
| OH M | $v = 8$ |

**Table 1.** Upper vibrational level populations included as free parameters in the spectral fitting.

The synthetic spectra described in the previous section provide wavelengths and relative intensities of thousands of individual rovibrational emission lines, which are combined to form a modelled spectrum for direct comparison with the HiTIES observations. To avoid making any assumptions about the vibrational distribution of GHOST emitting species, the populations of the upper vibrational levels of each molecule are independent free parameters in the fit to observations. Table 1 lists the upper vibrational levels of each band system which can produce emission within the range of the HiTIES observations and

https://doi.org/10.5194/egusphere-2025-5317
Preprint. Discussion started: 16 December 2025


are therefore included. To reduce the number of free parameters, it is assumed that all $N_2$ bands have the same rotational temperature, and the $N_2^+$ and $O_2^+$ bands also have the same rotational temperature (but this can be different to the neutral $N_2$ rotational temperature). The OH airglow spectrum is likely not related to the GHOST, and its rotational temperature is also a separate free parameter. In addition to the molecular band systems, the four emission lines of the $O^+$ ($^2D$–$^2P$) doublet close to 732 nm and 733 nm are included with two free parameters: the total intensity of these $O^+$ lines and the ratio of populations in the $J = 1/2$ and $J = 3/2$ levels of the $^2P$ upper state, which may be temperature dependent in aurora (Whiter et al., 2014). All line intensities are corrected to account for water vapour absorption in the lower atmosphere, following the method of Chadney et al. (2017), with the precipitable water vapour (PWV, effectively a column density) as a free parameter.

The final step in creating the modelled spectrum is to generate a Gaussian line profile for each emission line on the HiTIES detector (other profile shapes were also tested, but Gaussian provided the best results). The width of all Gaussians is the same (the instrument spectral resolution), and is a free parameter in the fit. Since the spectrograph slit appears curved in the image on the detector (Chakrabarti et al., 2001), the wavelength calibration varies slightly along the length of the slit. The observed HiTIES spectra presented here are generated by integrating along the length of the slit, but if the emitter does not fill the slit then the wavelength calibration will have a slight dependence on the position of the emitter within the slit. Therefore, we incorporate the wavelength calibration into the fitting process to obtain the most accurate results. The wavelength calibration is a polynomial function converting pixel number to wavelength, and contributes 5 free parameters to the fit. Similarly, the spatial extent of the emitter has a slight influence on the width of the Gaussian line profiles, which is why that width is also a free parameter.

| Property | Free parameters |
|---|---|
| Molecular vibrational populations (see Table 1) | 16 |
| Rotational temperatures | 3 |
| $O^+$ ($^2D$–$^2P$) lines | 2 |
| Water vapour absorption | 1 |
| Constant background | 1 |
| Gaussian line width (spectral resolution) | 1 |
| Wavelength calibration | 5 |
| Total | 29 |

**Table 2.** Summary of the free parameters in the spectral fitting process.

In total, the modelled spectrum is generated from 29 free parameters, summarised in Table 2. The modelled spectrum is fit to the data by minimising the weighted root-mean-square (RMS) of the residuals between the two, with weights provided by the errors on the HiTIES observations. Since there are many free parameters, there are many local minima in the parameter space, and so a gradient descent or similar algorithm is unlikely to find the global minimum (i.e. best fit). We therefore use a simulated annealing technique, first outlined in Kirkpatrick et al. (1983), which can escape local minima to find the global

https://doi.org/10.5194/egusphere-2025-5317
Preprint. Discussion started: 16 December 2025


minimum, but is time and computing intensive. This method is an iterative process. In each iteration, a random neighbouring state to the current state (i.e. similar set of parameter values) is selected and tested against the data. This new state is accepted if it provides an improved fit to the data, but can also be accepted if it provides a worse fit, according to how much worse it is (measured with the RMS) and a parameter called the annealing temperature, enabling the escape from local minima. The probability of accepting a worse state is initially high, but reduces with each iteration as the annealing temperature is reduced exponentially (system "cools"). The process ends either when no new state is accepted for 90 iterations or when a total of 3000 iterations (accepted or not) has been reached. The whole process is repeated 3 times, and the state with the lowest RMS from the full set of up to 9000 iterations is then chosen as the best fit to the data. This method was first used to fit synthetic spectra to HiTIES data by Price (2021), and is described in detail in a different context in their work.

### 4.3 Results

Spectral fitting of the HiTIES data shows the breakdown of different components of the spectrum, for different types of aurora observed on 03 Jan 2020, close to the GHOST event.

First, low energy precipitation from 08:02 UT is shown in Figure 4 (top). The spectral modelling shows typical auroral conditions on Svalbard, where the $O^+$ $^2P$ doublets are dominant. These are produced in the F-region by low energy precipitation. OH airglow and a small amount of $N_2$ 1P are also visible here. High-energy precipitation is shown in Figure 4 (bottom). The fitting shows a typical high-energy spectrum, with $N_2$ 1P being the dominant component. These results give a baseline of what is typically expected during 'normal' aurora.

Next, we present the results of fitting the confirmed GHOST spectrum in Figure 5 (top). There is still $O^+$ and $N_2$ 1P, but the $N_2$ IRA band system is significantly enhanced. The $N_2^+$ M and $O_2^+$ 1N are also enhanced as compared to the $N_2$ 1P. $N_2^+$ M seems to be especially important for the shape of the spectrum. Although $N_2$ IRA is normally weak, it does have vibrational bands through much of the visible and near infrared, at least for wavelengths longer than $\sim 520$ nm, and $N_2^+$ M could also cover the whole visible range if there is enough population in the high vibrational levels. The fitting of $N_2$ explains the full brightness of the continuum without any indication of the presence of NO.

Close to the continuum event, some 'normal' $N_2$ aurora was fitted, as shown in Figure 5 (bottom). In this spectrum, though $N_2$ 1P is dominant, there is an increased contribution from $N_2$ IRA and $N_2^+$ M. This could be continuum-like emission, representing the 'missing link' between normal aurora and GHOST. It could result from temperatures in between the typical values and the extreme heating found in GHOST events.

Besides the enhanced $N_2$ IRA in the continuum, another key difference to normal aurora is the rotational temperature. In the normal nightside high energy aurora the $N_2$ temperature was found to be 278 K, and the ion temperature ($N_2^+$ and $O_2^+$ rotational) came out at 162 K. This value has a high uncertainty due to the emission being relatively weak, but it nonetheless gives a good magnitude estimate. In contrast, the continuum fit gave an $N_2$ rotational temperature of 881 K, and an ion temperature of 2927 K, consistent with EISCAT ion temperature measurements above 150 km presented in Partamies et al. (2025).

https://doi.org/10.5194/egusphere-2025-5317
Preprint. Discussion started: 16 December 2025


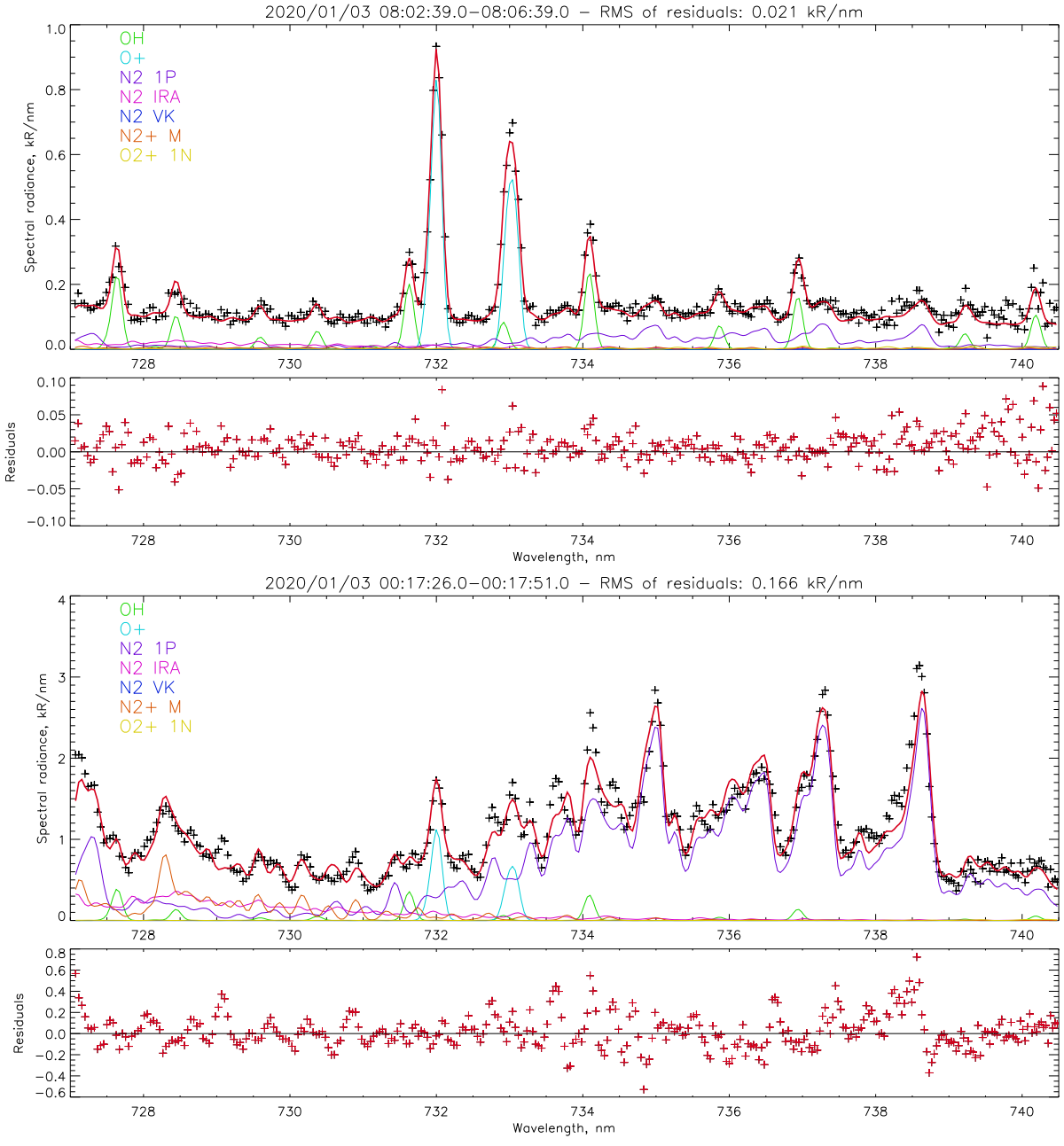


**Figure 4.** HiTIES spectrum of low-energy precipitation (top two panels, black plus symbols) on 03 Jan 2020 at 08:02 UT, and high-energy precipitation at 00:17 UT (bottom two panels) deconstructed into its spectral components; OH (green), $O^+$ (cyan), $N_2$ 1P (purple), $N_2$ IRA (magenta), $N_2$ VK (blue), $N_2^+$ M (orange) and $O_2^+$ 1N (yellow). The total fit (sum of all components) is plotted in red. Residuals plotted below.

https://doi.org/10.5194/egusphere-2025-5317
Preprint. Discussion started: 16 December 2025


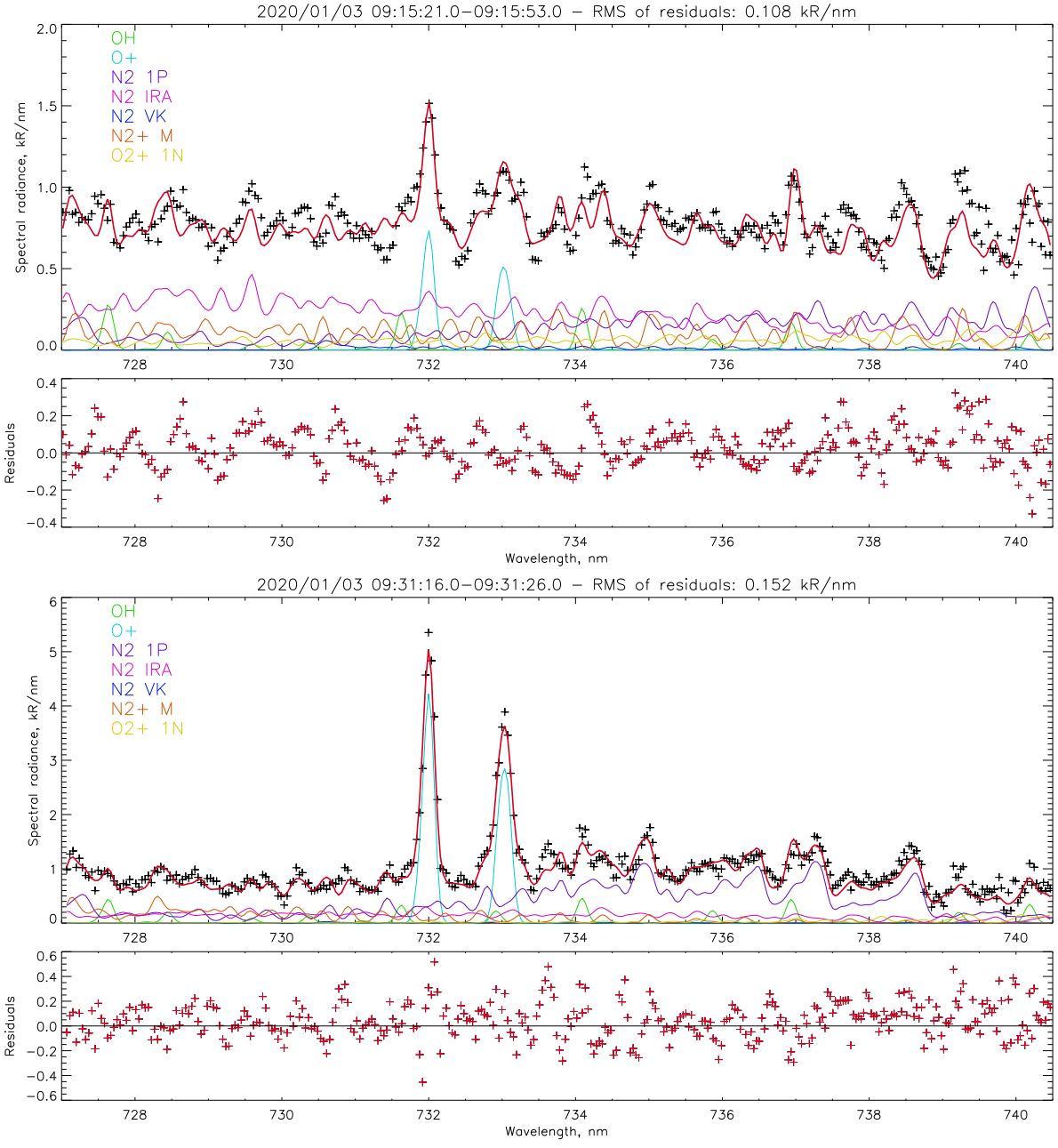


**Figure 5.** HiTIES spectrum of GHOST continuum (top two panels, black plus symbols) and low-energy precipitation with possible continuum contribution (bottom two panels), deconstructed into its spectral components; OH (green), $O^+$ (cyan), $N_2$ 1P (purple), $N_2$ IRA (magenta), $N_2$ VK (blue), $N_2^+$ M (orange) and $O_2^+$ 1N (yellow). The total fit (sum of all components) is plotted in red. Residuals plotted below.

https://doi.org/10.5194/egusphere-2025-5317
Preprint. Discussion started: 16 December 2025


These results indicate that the continuum emission is linked to strong heating. As 881 K is not that unusual in the thermosphere, it alone is therefore unlikely to be enough to thermally excite the $N_2$ IRA. However, it is an extreme temperature for the E-region. The high rotational temperatures generally flatten all band systems, which would make the spectrum more continuum-like at all wavelengths.

There is some structure visible in the residuals of Figure 4 (bottom) and both fits from Figure 5. This indicates that some of the components of the spectrum are not being correctly fitted — this could be due to a single temperature being assumed, whereas in reality the spectrum is made up of the entire integrated line-of-sight column and would thus contain a range of temperatures affecting the shape of the rotational spectrum for the $N_2$, $N_2^+$, and $O_2^+$ species when observed on the ground.

## 5 Background conditions

We also consider the global magnetospheric conditions during the GHOST events in order to begin to identify the conditions needed for GHOSTs to occur. GHOSTs have been observed at various magnetic local times (MLT) (Partamies et al., 2025). In this paper, the first and third events occur in the dawn–noon sector (9-12 MLT), and the second event occurs in the midnight–dawn sector (3-6 MLT). The IMF conditions for all three events can be found in Figure 6 and are discussed with the event descriptions below. Global ionospheric plasma convection patterns from the SuperDARN radar network can be found in Figure 7. The figure includes one convection map for each of our three GHOST events with flow vectors colour-coded by the flow velocity.

SuperDARN convection maps fit line of sight velocity from multiple radars to the map potential model in order to provide an empirical model view of polar cap electrostatic potential during that time (Ruohoniemi and Baker, 1998). Flow vectors are also inferred from the data and overplotted on the empirical model. Due to radar distribution, there is minimal backscatter and therefore minimal data available above Svalbard, however convection maps are still presented in order for discussion of the polar cap equipotential cells and global convection behaviour during the GHOST events.

### 5.1 Event 1: 03 January 2020

During Event 1, the ESR 32 metres dish was run on a program pointing north at an elevation of 30°. This enabled ESR to capture pulsed ionospheric flows (PIFs, also sometimes referred to in literature as poleward moving radar auroral forms), which are the ionospheric signatures of energetic flux transfer events (FTEs) evidencing energetic pulsed reconnection at the dayside magnetopause. These are circled in Figure 8 as ion velocity enhancements appearing at ∼350 km and moving further in range in the radar beam at about 08:30, 09:00, 09:30, 09:45 UT. This would place Event 1 from 8:30-9:30 UT firmly in the cusp ionosphere.

Partamies et al. (2025) reported observation of patchy or pulsing proton aurora during Event 1. Previous work on patchy proton events on Svalbard has concluded that they are evidence of FTEs (Moen et al., 1998; Deehr and Lummerzheim, 2001), which also locates this event in the cusp. It is further interesting to note that the IMF is mostly Bz-negative throughout the ob-

https://doi.org/10.5194/egusphere-2025-5317
Preprint. Discussion started: 16 December 2025


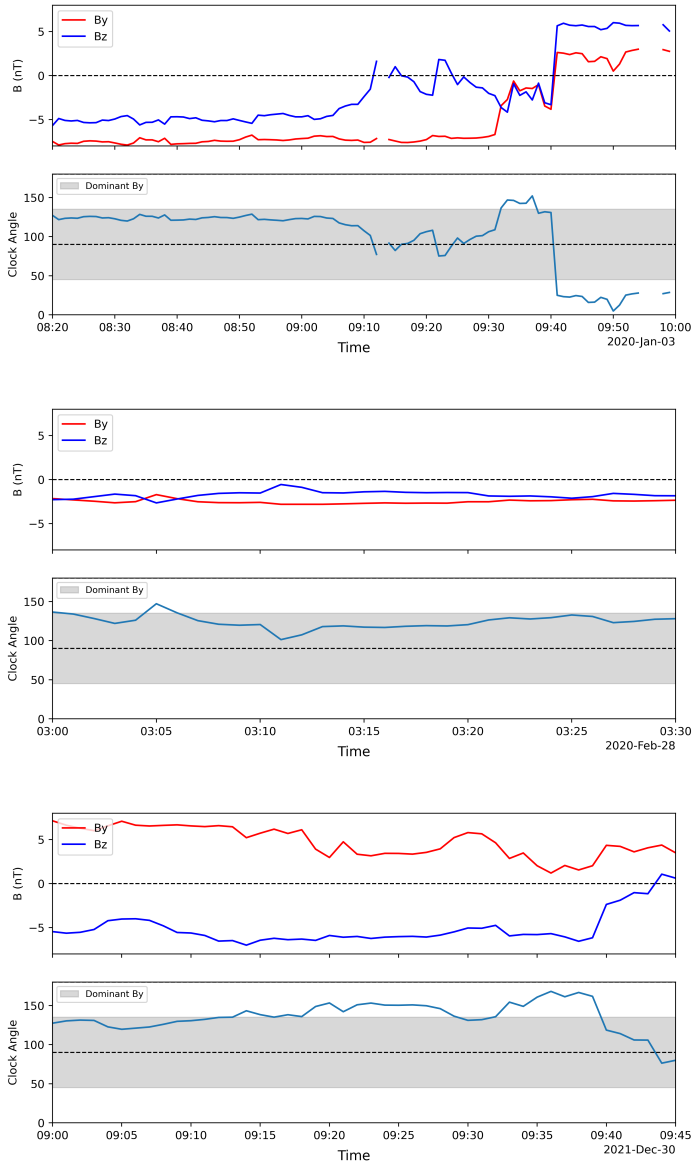


**Figure 6.** IMF conditions on the 03 Jan 2020 (top), 28 Feb 2020 (middle), and 30 Dec 2021 (bottom), showing IMF Bz, By, clock angle, and the associated clock angle region where By is dominant. By dominance is defined as the range of clock angles of the solar wind with angles between 45 and 135°.

servation interval, an IMF orientation which leads to the most energetic reconnection and therefore most energetic precipitation into the cusp ionosphere.

https://doi.org/10.5194/egusphere-2025-5317
Preprint. Discussion started: 16 December 2025


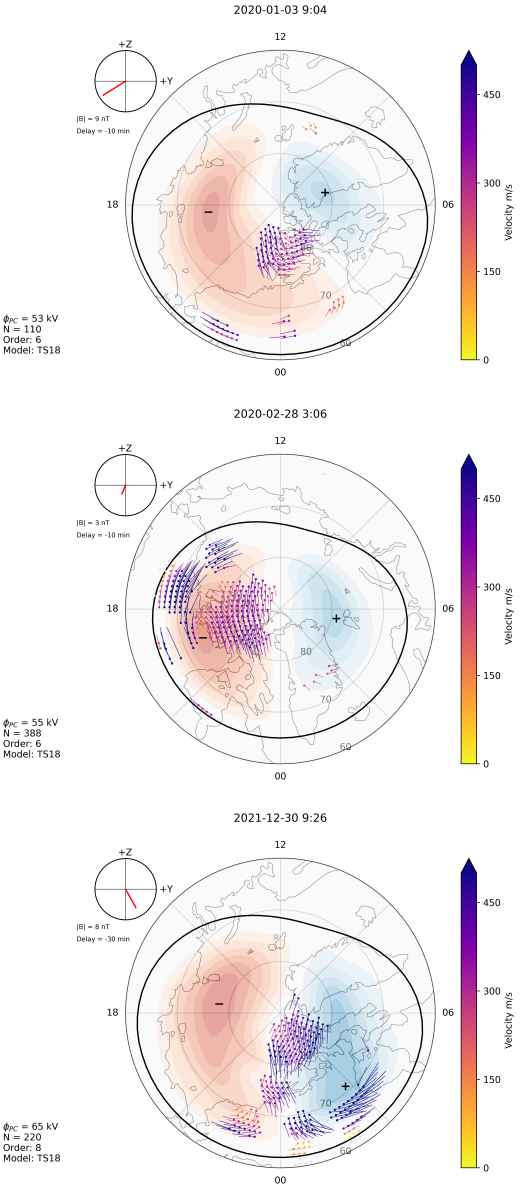


**Figure 7.** SuperDARN global polar cap convection map data from times during the GHOST events on 03 Jan 2020 (top) and 21 Feb 2020 (middle) and 30 Dec 2021 (bottom). Flow velocity vectors are shown by ball and stick plots with colour maps. Equipotential polar cap cells are blue (negative) and red (positive). The Heppner-Maynard boundary representing the equatorward edge of the high-latitude ionospheric model convection pattern is shown in black.

Supplementary material of this event from Partamies et al. (2025) includes a video in which the GHOST is seen flowing eastwards. This eastwards flow is consistent with cusp flow in the dominant negative By regime (Burch et al., 1985; Lockwood

https://doi.org/10.5194/egusphere-2025-5317
Preprint. Discussion started: 16 December 2025


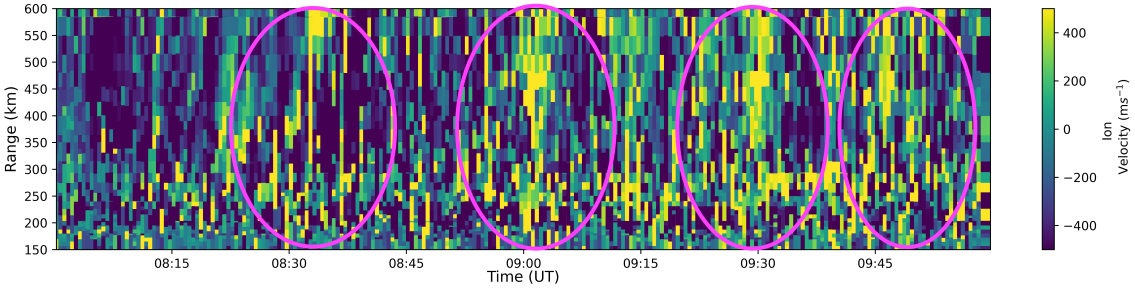


**Figure 8.** ESR 32m data at 30 degree elevation (pointed poleward) from 08:00-10:00 UT on 03/01/2020. PIF signatures are identified (circled in pink) in the ion drift velocity as slanted increases in the ion velocity moving further in range (and thus poleward) with time.

et al., 1989), which is consistent with IMF conditions in Figure 6. Dominant By conditions are also visible in the modelled equipotential polar cap cells in Figure 7, which would place the convection throat over Svalbard.

Finally, we note that the corresponding GHOST arc seen in this event is broad and the thickest of the three events presented in this paper, suggesting that the prevailing conditions were the most favourable.

### 5.2 Event 2: 28 February 2020

The morning sector GHOST on 28 February 2020 occurs at about 03 UT (about 06 MLT), and we do not see any patchy protons or other reconnection signatures at that MLT, as expected as the observations are not in the cusp. However, similar to the previous event, referring to the middle panel in Figure 6, the event takes place during a period of dominant By with negative Bz. It is interesting to note that there appears to be stronger ionospheric return flows in SuperDARN (Figure 7) than cross-polar cap (antisunward) flows at this time. With the expected polar cap asymmetry under dominant By conditions as outlined in Cowley and Lockwood (1992), and judging by the contour lines of the equipotential polar cap cells as seen in the middle panel of Figure 7, it is possible that Svalbard is located underneath a similar strong return flow. In supplementary material provided, the GHOST in event 2 is seen flowing eastwards, consistent with the direction of a strong return flow over Svalbard.

The presence of a strong flow over Svalbard at the time of GHOST observation is indicated by considering data from the International Monitor for Auroral Geomagnetic Effects (IMAGE) magnetometer network (Tanskanen, 2009), presented in Figure 9. There is an observable dip in the X-component at the time of the GHOST (∼03 UT) which would indicate an enhancement of the westwards electrojet, thus enhanced return flow convection in the dawn sector above Svalbard at the time the GHOST is observed.

It is noted that Event 2 is thinner compared to its Event 1 counterpart, suggesting less favourable conditions than Event 1.

### 5.3 Event 3: 30 December 2021

Event 3, like Event 1, takes place in the sunlit dayside ionosphere. Also similar to Event 1, there are patchy proton aurora during Event 3 visible in Figure A1, consistent with cusp conditions and energetic dayside reconnection. Referring to the

https://doi.org/10.5194/egusphere-2025-5317
Preprint. Discussion started: 16 December 2025


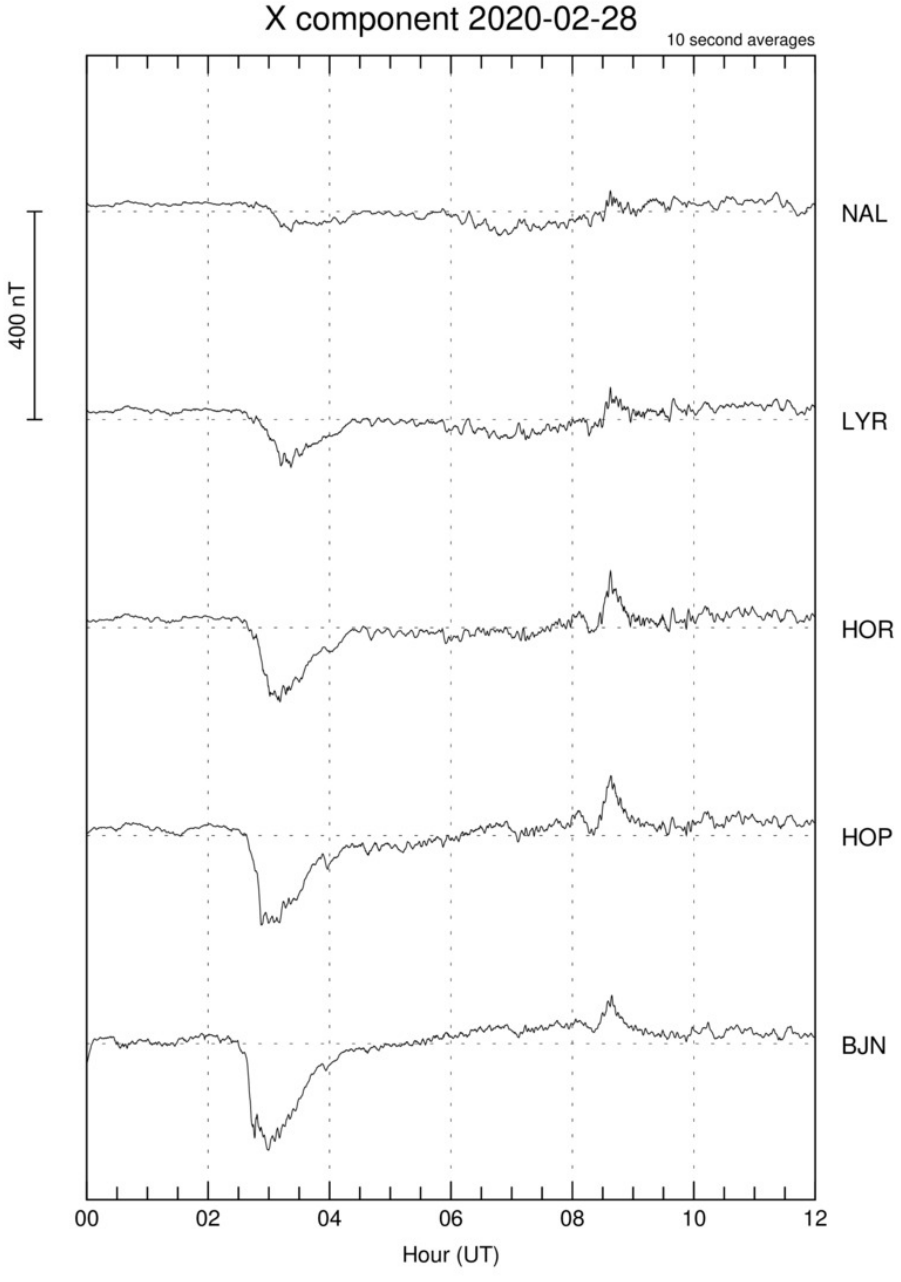


**Figure 9.** IMAGE data from the Svalbard magnetometers (Ny-Ålesund (NAL), Longyearbyen (LYR), Hornsund (HOR), Hopen Island (HOP), Bear Island (BJN)) showing the variation in the X component in 10 second averages from 0-12 UT on 28 February 2020. An enhancement of the westwards electrojet is visible around ∼03 UT as a sharp decrease in the X component.

https://doi.org/10.5194/egusphere-2025-5317
Preprint. Discussion started: 16 December 2025


bottom panel of Figure 6, like Events 1 and 2, Bz was negative throughout the event. Unlike Event 1, the By component was not fully dominant throughout the time period of interest. Again, there is no backscatter from SuperDARN radars near Svalbard, as seen in the bottom panel of Figure 7. The convection map shows a cross-polar cap flow originating from dayside reconnection, but unlike in Event 1, there does not appear to be strongly dominant By influence on the polar cap convection cells. Indeed, looking at Figure 6, By is only slightly dominant for the interval immediately prior to the GHOST observation and is not dominant during the observation period of the GHOST from 9:12 - 9:33 UT.

In the supplementary material, the GHOST is seen flowing westwards. It is interesting to note IMF By has opposite polarity from Event 1, which would be consistent with opposite-direction flow. The GHOST is noted to be off-zenith, so it is not possible to reliably judge the thickness of its structures.

### 5.4 Summary of Background Conditions

Examining the background conditions from across the three events presented in this paper, a certain number of factors can be identified as possibly influencing the appearance of the GHOST. These factors across the events, as well as the type of GHOST observed, are presented in Table 3.

| Event | Type of GHOST | GHOST Flow Direction | By Polarity | By Dominance | Bz | Cusp | Energetic Dayside Reconnection | Sunlit |
|---|---|---|---|---|---|---|---|---|
| 03 Jan 2020 | Broad | East | -ve | Yes | -ve | Yes | Yes | Yes |
| 28 Feb 2020 | Thin | East | -ve | Yes | -ve | No | N/A | No |
| 30 Dec 2021 | Off-zenith | West | +ve | No | -ve | Yes | Yes | Yes |

**Table 3.** Summary of GHOST events presented in this paper and their associated background conditions.

## 6 Proposed mechanism

We propose that the GHOST continuum emission requires an ionosphere that is primed with upwelling, heating, and excitation of $N_2$, $N_2^+$ and $O_2^+$. When precipitation collides with this primed ionosphere, continuum made up of electronically and vibrationally excited $N_2$, $N_2^+$ and $O_2^+$ is emitted. Figure 10 shows a cartoon of the combination of background conditions observed, as discussed here.

The cusp regions are important to this priming due to the steady input of the low energy electrons, which can efficiently heat the ionosphere. The largest known GHOST events, such as Event 1 in this study and another dayside event reported by Partamies et al. (2025), occurred co-located and simultaneously with cusp signatures such as patchy proton aurora, poleward moving auroral forms, and FTE signatures. As the cusps heat the dayside ionosphere with the low-energy electron precipitation, it causes upwelling of lower ionospheric species to altitudes higher than the shadow height.

The cusp region GHOST occurrences also place the GHOST processes in the sunlit ionosphere, which is seen as an enhanced glow of the blue emission from molecular nitrogen ions, the resonance scattering. Above the shadow height, sunlight

https://doi.org/10.5194/egusphere-2025-5317
Preprint. Discussion started: 16 December 2025


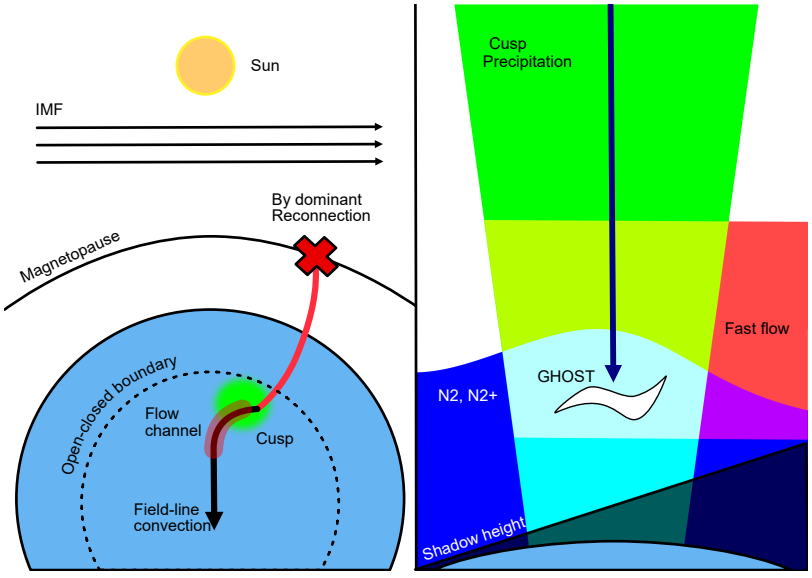


**Figure 10.** Cartoon of proposed continuum mechanism showing how the background conditions evidenced could combine to produce GHOST conditions. The left panel (view from above into the polar region) shows how the solar wind conditions result in flow channels close to local noon. The right panel (view from the dusk side into the vertical cross-section of the cusp ionosphere) shows how the cusp location, flow channel, and upwelling of $N_2$ combine, each contributing to prime the ionosphere to produce GHOST emissions.

contributes to the ionisation of the upwelled species. Particularly the abundance of $N_2^+$ tends to peak around the height of about 160 km, because below that the lifetime of this ion sharply decreases (Hunten, 2003). The sunlit ionosphere therefore together with the upwelling has been deemed as an important ingredient for the GHOST background conditions.

The known large and persistent GHOST events take place during By dominant, southward IMF. This is true for Events 1 and 2 in this study, as well as for another dayside event discussed in Partamies et al. (2025) (∼06 UT on 11 February 2024). Under By-dominant IMF conditions the cusp will either be dawnward (as depicted in Figure 10) or duskward of noon. After reconnecting, field-lines must therefore convect meridionally noonwards before they convect across the polar cap from noon to midnight. These conditions produce strong east-west flow channels on the dayside, providing strong frictional heating. A horizontal shear flow was observed in connection to the GHOST aurora in Partamies et al. (2025), suggesting that this additional frictional heating may also play a key role in setting the GHOST conditions.

The brightest, largest and longest-lived GHOST aurora observed so far appear during these ideally primed conditions where the ionosphere is hot, expanded, and sunlit. We propose that the combination of these energy sources produces a (pseudo-)continuum spectrum by exciting the $N_2$ IRA, $N_2^+$ M, and $O_2^+$ 1N band systems. These band systems are present throughout the whole visible range. The upwelled $N_2$, $N_2^+$ and $O_2^+$ in this scenario can be abundant enough to produce the observed brightness of the broadband emission.

https://doi.org/10.5194/egusphere-2025-5317
Preprint. Discussion started: 16 December 2025


## 7 Conclusions

GHOST emissions produce a pseudo-continuum, visually similar to STEVE and other continuum auroral features. Previous studies have suggested that the NO mechanism is responsible for observations of GHOST pseudo-continuum, but it faces significant challenges to have a high enough rate of production of NO to explain the observed brightness.

The high-resolution spectra observations shown in this study are the first attempt to unpick the continuum spectrum at the level of the rotational structure of the band systems. Fitting shows that the continuum spectrum can be deconstructed into $N_2$ first positive as expected, but with a significant contribution from the $N_2$ infra-red afterglow band system, the $N_2^+$ Meinel system, and the $O_2^+$ first negative system. The infra-red afterglow and Meinel bands have not been considered in previous studies, and produce emission throughout the visible range. We propose that a combination of these high energy, vibrationally excited states could be a possible explanation for the continuum emissions within the auroral oval, without the need for high levels of NO.

To determine the origin of the energy required to produce these highly energised molecules, we look at the background conditions common to GHOST events. Extreme ion temperatures and high neutral temperatures are evidenced by spectral fitting, supported by measurements reported in Partamies et al. (2025). We find that soft cusp precipitation and daylit ionosphere conditions are present in the brightest GHOST events. IMF conditions with dominant By and southward Bz are also identified as possible contributors, as these conditions result in strong high-latitude global flows and direct energetic reconnection flow into the ionosphere respectively. We suggest that these are the origins of strong flow and shear conditions identified by DMSP measurements in Partamies et al. (2025).

We propose that the combination of upwelling, heating, and shear flow provides the energy needed to excite the $N_2$, $N_2^+$, and $O_2^+$ to produce the observed pseudo-continuum. This provides a unified explanation of GHOST and other continuum auroral emissions, and we provide evidence of a possible in-between state.

Future work should produce more detailed modelling, including additional band systems, atmospheric species, and exploring the full observed range of continuum wavelengths. Comparing modelled spectra with MISS could test whether these $N_2$ band systems provide the full brightness of the spectrum over a wider wavelength range than the HiTIES observations allow. Statistical studies exploring GHOST occurrence and intensity with solar wind, ionospheric flow, and cusp conditions would be valuable, particularly in investigating the shear flow and heating thresholds required to produce continuum. The emission altitude could be constrained by multi-instrument and/or citizen science imagery of GHOST. The combined heating factors resulting in excited $N_2$ could also be investigated as contributors to the spectrum of STEVE and other auroral continuum emissions.

*Code and data availability.* Software for wavelength calibration and plotting of MISS data is available at https://github.com/UNISvalbard/KHO-MISS/ (Syrjäsuo, 2025). SuperDARN Data was accessed through the British Antarctic Survey. Other SuperDARN data mirrors are available via the Virginia Tech SuperDARN group and the University of Saskatchewan. The Radar Software Toolkit (RST) to process the SuperDARN data can be downloaded from https://github.com/SuperDARN/rst (SuperDARN Data Analysis Working Group. Participating Members et al.,

https://doi.org/10.5194/egusphere-2025-5317
Preprint. Discussion started: 16 December 2025


2018). pyDARN, an open source python library for data visualization of SuperDARN data, was used for the production of the plots in this paper and can be downloaded from https://github.com/SuperDARN/pydarn (SuperDARN Data Visualization Working Group et al., 2025).

EISCAT data are available through the CEDAR Madrigal database (http://cedar.openmadrigal.org, Rideout and Cariglia 2025)

The HiTIES data used in the study are publicly available at https://www.soton.ac.uk/~dkw1f08/HiTIES_GHOST.zip (to be replaced with a DOI on acceptance).

*Video supplement.* Video supplement from the UNIS all-sky camera is available for Event 2 and Event 3, to show the flow direction of auroral forms as well as the evolution of the GHOST event at the following locations https://www.soton.ac.uk/~dkw1f08/Event2-28022020_0213.avi, https://www.soton.ac.uk/~dkw1f08/Event2-28022020_0314.avi, https://www.soton.ac.uk/~dkw1f08/Event3-30122021.avi (to be replaced with a DOI on acceptance of the paper).

## Appendix A: Patchy proton observations during Event 3

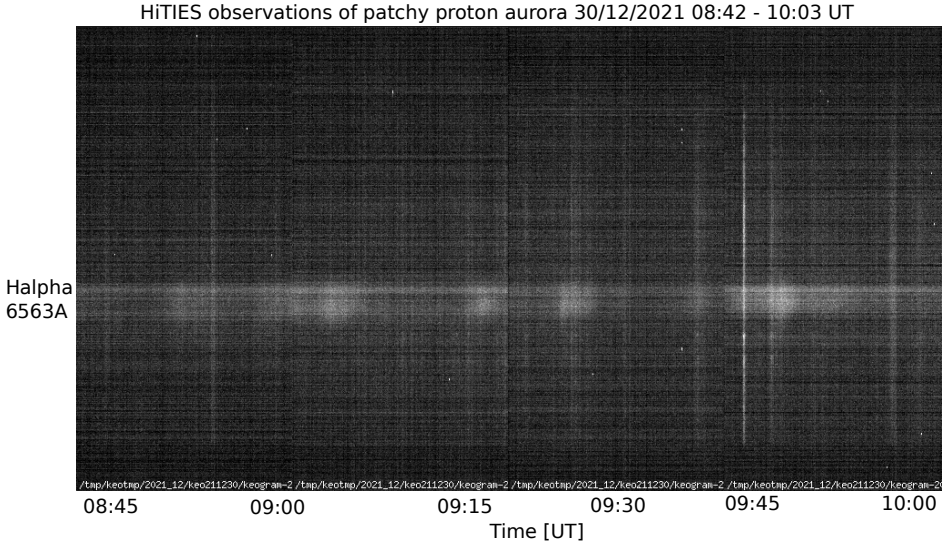


**Figure A1.** Keogram of HiTIES observations of proton aurora from 08:42 to 10:03 UT on 30/12/2021 during GHOST event 3. Bursts of proton aurora appear as broad bright blobs, blue-shifted from the H$\alpha$ wavelength at 08:50, 09:00, 09:17, 09:28, and 09:47 UT

*Author contributions.* RD and FB jointly developed the main concepts of this study. RD, FB, SS, and NP wrote most of the manuscript. RD led the study, performed the preliminary spectral identification, identified events, and led the writing. FB analysed the background conditions. DKW carried out the spectral fitting of HiTIES data, and assisted in developing the main concepts. SS performed the spectral modelling.

https://doi.org/10.5194/egusphere-2025-5317
Preprint. Discussion started: 16 December 2025


NP identified events, analysed MISS spectra and all-sky images. MB investigated contributions from $NO_2$. KH and EK contributed to the discussion and development of the study. All authors contributed to the discussion, interpretation, and the preparation of the manuscript.

*Competing interests.* The authors declare that they have no conflict of interest.

*Acknowledgements.* This research was supported by the International Space Science Institute (ISSI) in Bern through the ISSI Working Group project ARCTICS. The authors acknowledge the use of SuperDARN data. SuperDARN is a collection of radars funded by national scientific funding agencies of Australia, Canada, China, France, Italy, Japan, Norway, South Africa, United Kingdom and the United States of America. We thank the institutes who maintain the IMAGE Magnetometer Array: Tromsø Geophysical Observatory of UiT the Arctic University of Norway (Norway), Finnish Meteorological Institute (Finland), Institute of Geophysics Polish Academy of Sciences (Poland), GFZ German Research Centre for Geosciences (Germany), Geological Survey of Sweden (Sweden), Swedish Institute of Space Physics (Sweden), Sodankylä Geophysical Observatory of the University of Oulu (Finland), DTU Technical University of Denmark (Denmark), and Science Institute of the University of Iceland (Iceland). The provisioning of data from AAL, GOT, HAS, NRA, VXJ, FKP, SIN, BOR, SCO and KUL is supported by the ESA contracts number 4000128139/19/D/CT as well as 4000138064/22/D/KS. The operation and maintenance of the HiTIES instrument has been funded by the Natural Environment Research Council (NERC) of the UK under grants NE/N004051/1 and NE/S015167/1. Rowan Dayton-Oxland was supported by NERC of the UK (grant no. NE/S007210/1). Fiona Ball was supported by the UK's Science and Technology Facilities Council (STFC) through studentship ST/Y509565/1 (2890595). Daniel Whiter and Srimoyee Samaddar were supported by NERC under grant NE/W003007/1. Noora Partamies was supported by Norwegian Research Council under the contract 354137 and 358004. Katie Herlingshaw was supported by Norwegian Research Council under the contract 343302 and 358004. Eero Karvinen was supported by the Magnus Ehrnrooth foundation. The authors thank the KHO ASC and MISS PIs Dag Lorentzen and Fred Sigernes for the data used in this study.

https://doi.org/10.5194/egusphere-2025-5317
Preprint. Discussion started: 16 December 2025


## References

Archer, W. E., Gallardo-Lacourt, B., Perry, G. W., St.-Maurice, J. P., Buchert, S. C., and Donovan, E.: STEVE: The Optical Signature of Intense Subauroral Ion Drifts, Geophysical Research Letters, 46, 6279–6286, https://doi.org/10.1029/2019GL082687, 2019.

Bates, D. R.: Cause of terrestrial nightglow continuum, Proceedings of the Royal Society of London. Series A: Mathematical and Physical Sciences, 443, 227–237, https://doi.org/10.1098/rspa.1993.0141, 1993.

Benesch, W., Rivers, D., and Moore, J.: High resolution spectrum of the $N_2^+$ Meinel system to 11 250 Å, Journal of the Optical Society of America, 70, 792–799, 1980.

Brooke, J. S., Bernath, P. F., Western, C. M., Sneden, C., Afşar, M., Li, G., and Gordon, I. E.: Line strengths of rovibrational and rotational transitions in the $X^2\Pi$ ground state of OH, J. Quant. Spectrosc. Radiat. Transfer, 168, 142–157, https://doi.org/10.1016/j.jqsrt.2015.07.021, 2016.

Budó, A.: Rotationsstruktur von $^4\Sigma \rightarrow ^4\Pi$-Banden, Zeitschrift für Physik, 105, 73–80, 1937.

Burch, J. L., Reiff, P. H., Menietti, J. D., Heelis, R. A., Hanson, W. B., Shawhan, S. D., Shelley, E. G., Sugiura, M., Weimer, D. R., and Winningham, J. D.: IMF $B_y$-dependent plasma flow and Birkeland currents in the dayside magnetosphere: 1. Dynamics Explorer observations, Journal of Geophysical Research: Space Physics, 90, 1577–1593, https://doi.org/10.1029/ja090ia02p01577, 1985.

Carroll, P. and Rubalcava, H.: Near Infra-Red System of Nitrogen, Nature, 184, 119–120, 1959.

Carroll, P. and Rubalcava, H.: Rotational Analysis of the 5-1 Band of the B'-B System of $N_2$, Proceedings of the Physical Society, 76, 337, 1960.

Carroll, P. and Sayers, N.: The Band Spectrum of Nitrogen: New Studies of the Triplet Systems, Proceedings of the Physical Society. Section A, 66, 1138, 1953.

Chadney, J. M., Whiter, D. K., and Lanchester, B. S.: Effect of water vapour absorption on hydroxl temperatures measured from Svalbard, Ann. Geophys, 35, 481–491, https://doi.org/10.5194/angeo-35-481-2017, 2017.

Chakrabarti, S., Pallamraju, D., Baumgardner, J., and Vaillancourt, J.: HiTIES: A High Throughput Imaging Echelle Spectrogragh for ground-based visible airglow and auroral studies, Journal of Geophysical Research: Space Physics, 106, 30 337–30 348, https://doi.org/10.1029/2001JA001105, 2001.

Cowley, S. W. H. and Lockwood, M.: Excitation and decay of solar wind-driven flows in the magnetosphere-ionosphere system, Annales Geophysicae, 10, 103–115, 1992.

Deehr, C. and Lummerzheim, D.: Ground-based optical observations of hydrogen emission in the auroral substorm, Journal of Geophysical Research: Space Physics, 106, 33–44, https://doi.org/10.1029/2000JA002010, 2001.

Evans, W. F., Gattinger, R. L., Slanger, T. G., Saran, D. V., Degenstein, D. A., and Llewellyn, E. J.: Discovery of the FeO orange bands in the terrestrial night airglow spectrum obtained with OSIRIS on the Odin spacecraft, Geophysical Research Letters, 37, https://doi.org/10.1029/2010GL045310, 2010.

Gillies, D. M., Donovan, E., Hampton, D., Liang, J., Connors, M., Nishimura, Y., Gallardo-Lacourt, B., and Spanswick, E.: First Observations From the TREx Spectrograph: The Optical Spectrum of STEVE and the Picket Fence Phenomena, Geophysical Research Letters, 46, 7207–7213, https://doi.org/10.1029/2019GL083272, 2019.

Gilmore, F. R., Laher, R. R., and Espy, P. J.: Franck–Condon factors, r-centroids, electronic transition moments, and Einstein coefficients for many nitrogen and oxygen band systems, Journal of Physical and Chemical Reference Data, 21, 1005–1107, 1992.

https://doi.org/10.5194/egusphere-2025-5317
Preprint. Discussion started: 16 December 2025


Goertz, C. K., Nielsen, E., Korth, A., Glassmeier, K. H., Haldoupis, C., Hoeg, P., and Hayward, D.: Observations of a possible ground signature of flux transfer events, Journal of Geophysical Research: Space Physics, 90, 4069–4078, https://doi.org/10.1029/JA090iA05p04069, 1985.

Greenwald, R. A., Baker, K. B., Dudeney, J. R., Pinnock, M., Jones, T. B., Thomas, E. C., Villain, J. P., Cerisier, J. C., Senior, C., Hanuise, C., Hunsucker, R. D., Sofko, G., Koehler, J., Nielsen, E., Pellinen, R., Walker, A. D., Sato, N., and Yamagishi, H.: DARN/SuperDARN - A global view of the dynamics of high-latitude convection, Space Science Reviews, 71, 761–796, https://doi.org/10.1007/BF00751350, 1995.

Harding, B. J., Mende, S. B., Triplett, C. C., and Wu, Y. J. J.: A Mechanism for the STEVE Continuum Emission, Geophysical Research Letters, 47, https://doi.org/10.1029/2020GL087102, 2020.

Herlingshaw, K., Partamies, N., van Hazendonk, C. M., Syrjäsuo, M., Baddeley, L. J., Johnsen, M. G., Eriksen, N. K., McWhirter, I., Aruliah, A., Engebretson, M. J., et al.: Science highlights from the Kjell Henriksen Observatory on Svalbard, Arctic Science, 11, 1–25, 2024.

Herzberg, G.: Molecular Spectra and Molecular Structure, vol. 1 - Spectra of Diatomic Molecules, Krieger Publishing Company, Malabar, Florida, 2nd edn., 1950.

Huber, K. P. and Herzberg, G. H.: "Constants of Diatomic Molecules" (data prepared by Jean W. Gallagher and Russell D. Johnson, III), in: NIST Chemistry WebBook, NIST Standard Reference Database Number 69, Eds. P.J. Linstrom and W.G. Mallard, National Institute of Standards and Technology, Gaithersburg MD, 20899, https://doi.org/https://doi.org/10.18434/T4D303.

Hunten, D. M.: Sunlit aurora and the $N_2^+$ ion: a personal perspective, Planetary and Space Science, 51, 887–890, https://doi.org/10.1016/S0032-0633(03)00079-5, 2003.

Jokiaho, O.-P.: Spectral modelling of molecular nitrogen in aurora, Ph.D. thesis, University of Southampton, 2009.

Kaplan, J.: New band system in nitrogen, Physical Review, 45, 675, 1934.

King, J. H. and Papitashvili, N. E.: Solar wind spatial scales in and comparisons of hourly Wind and ACE plasma and magnetic field data, Journal of Geophysical Research: Space Physics, 110, https://doi.org/10.1029/2004JA010649, 2005.

Kirkpatrick, S., Gelatt, C. D., and Vecchi, M. P.: Optimization by Simulated Annealing, Science, 220, 671–680, https://doi.org/10.1126/SCIENCE.220.4598.671, 1983.

Laher, R. R. and Gilmore, F. R.: Improved fits for the vibrational and rotational constants of many states of nitrogen and oxygen, Journal of Physical and Chemical Reference Data, 20, 685–712, 1991.

Liang, J. and Donovan, E.: Quantum Calculation of the Vibrational Excitation of Nitrogen Molecules by Fast Ions: Can It Contribute to STEVE Formation?, Geophysical Research Letters, 51, https://doi.org/10.1029/2024GL110986, 2024.

Liang, J., Donovan, E., Connors, M., Gillies, D., St-Maurice, J. P., Jackel, B., Gallardo-Lacourt, B., Spanswick, E., and Chu, X.: Optical Spectra and Emission Altitudes of Double-Layer STEVE: A Case Study, Geophysical Research Letters, 46, 13 630–13 639, https://doi.org/10.1029/2019GL085639, 2019.

Lockwood, M., Sandholt, P., Cowley, S., and Oguti, T.: Interplanetary magnetic field control of dayside auroral activity and the transfer of momentum across the dayside magnetopause, Planetary and Space Science, 37, 1347–1365, https://doi.org/10.1016/0032-0633(89)90106-2, 1989.

MacDonald, E. A., Donovan, E., Nishimura, Y., Case, N. A., Megan Gillies, D., Gallardo-Lacourt, B., Archer, W. E., Spanswick, E. L., Bourassa, N., Connors, M., Heavner, M., Jackel, B., Kosar, B., Knudsen, D. J., Ratzlaff, C., and Schofield, I.: New science in plain sight: Citizen scientists lead to the discovery of optical structure in the upper atmosphere, Science Advances, 4, https://doi.org/10.1126/sciadv.aaq0030, 2018.

https://doi.org/10.5194/egusphere-2025-5317
Preprint. Discussion started: 16 December 2025


Meinel, A.: A New Band System of $N_2^+$ in the Infrared Auroral Spectrum., Astrophysical Journal, 112, 562, 1950.

Meinel, A. B.: Origin of the Continuum in the Night-Sky Spectrum., The Astrophysical Journal, 118, 200, https://doi.org/10.1086/145742, 1953.

Mende, S. B., Harding, B. J., and Turner, C.: Subauroral Green STEVE Arcs: Evidence for Low-Energy Excitation, Geophysical Research Letters, 46, 14 256–14 262, https://doi.org/10.1029/2019GL086145, 2019.

Mishin, E. and Streltsov, A.: On the Kinetic Theory of Subauroral Arcs, Journal of Geophysical Research: Space Physics, 127, e2022JA030 667, https://doi.org/10.1029/2022JA030667, 2022.

Moen, J., Lorentzen, D. A., and Sigernes, F.: Dayside moving auroral forms and bursty proton auroral events in relation to particle boundaries observed by NOAA 12, Journal of Geophysical Research: Space Physics, 103, 14 855–14 863, https://doi.org/10.1029/97ja02877, 1998.

Nanjo, S., Hofstra, G. A., Shiokawa, K., Shinbori, A., Nozawa, S., and Hosokawa, K.: Post-midnight purple arc and patches appeared on the high latitude part of the auroral oval: Dawnside counterpart of STEVE?, Earth, Planets and Space, 76, https://doi.org/10.1186/s40623-024-01995-9, 2024.

Naudé, S. M.: The Rotational Analysis of the First Positive Nitrogen ($N_2$) Bands, Physical Review, 38, 372, 1931.

Nicholls, R. and Stewart, A.: Atomic and molecular processes, Academic Press Inc., New York, N. Y, 1962.

Noll, S., Plane, J. M. C., Feng, W., Kalogerakis, K. S., Kausch, W., Schmidt, C., Bittner, M., and Kimeswenger, S.: Structure, variability, and origin of the low-latitude nightglow continuum between 300 and 1800 nm: evidence for $HO_2$ emission in the near-infrared, Atmospheric Chemistry and Physics, 24, 1143–1176, https://doi.org/10.5194/acp-24-1143-2024, 2024.

Partamies, N., Dayton-Oxland, R., Herlingshaw, K., Virtanen, I., Gallardo-Lacourt, B., Syrjäsuo, M., Sigernes, F., Nishiyama, T., Nishimura, T., Barthelemy, M., Aruliah, A., Whiter, D., Mielke, L., Grandin, M., Karvinen, E., Spijkers, M., and Ledvina, V.: First observations of continuum emission in dayside aurora, Annales Geophysicae, 43, 349–367, https://doi.org/10.5194/angeo-43-349-2025, 2025.

Pinnock, M., Rodger, A. S., Dudeney, J. R., Baker, K. B., Newell, P. T., Greenwald, R. A., and Greenspan, M. E.: Observations of an enhanced convection channel in the cusp ionosphere, Journal of Geophysical Research: Space Physics, 98, 3767–3776, https://doi.org/10.1029/92JA01382, _eprint: https://onlinelibrary.wiley.com/doi/pdf/10.1029/92JA01382, 1993.

Price, D. J.: Observations of thermospheric heating signatures associated with sub-kilometer scale auroral electrodynamics, Ph.D. thesis, University of Southampton, Southampton, https://eprints.soton.ac.uk/455066/, 2021.

Rideout, W. and Cariglia, K.: CEDAR Madrigal Database [data set], https://cedar.openmadrigal.org, last access: 26 October 2025, 2025.

Ruohoniemi, J. M. and Baker, K. B.: Large-scale imaging of high-latitude convection with Super Dual Auroral Radar Network HF radar observations, Journal of Geophysical Research: Space Physics, 103, 20 797–20 811, https://doi.org/10.1029/98ja01288, 1998.

Sandholt, P. E., Deehr, C. S., Egeland, A., Lybekk, B., Viereck, R., and Romick, G. J.: Signatures in the dayside aurora of plasma transfer from the magnetosheath, Journal of Geophysical Research: Space Physics, 91, 10 063–10 079, https://doi.org/10.1029/JA091iA09p10063, _eprint: https://onlinelibrary.wiley.com/doi/pdf/10.1029/JA091iA09p10063, 1986.

Sandholt, P. E., Moen, J., and Opsvik, D.: Periodic auroral events at the midday polar cap boundary: Implications for solar wind-magnetosphere coupling, Geophysical Research Letters, 19, 1223–1226, https://doi.org/10.1029/92GL01275, _eprint: https://onlinelibrary.wiley.com/doi/pdf/10.1029/92GL01275, 1992.

Schadee, A.: The formation of molecular lines in the solar spectrum, Bulletin of the Astronomical Institutes of the Netherlands, 17, 311–357, 1964.

Shemansky, D. E. and Vallance Jones, A.: Type-B red aurora; The $O_2^+$ first negative system and the $N_2$ first positive system, Planetary and Space Science, 16, 1115–1130, https://doi.org/10.1016/0032-0633(68)90124-4, 1968.

https://doi.org/10.5194/egusphere-2025-5317
Preprint. Discussion started: 16 December 2025


Shiokawa, K., Otsuka, Y., and Connors, M.: Statistical Study of Auroral/Resonant-Scattering 427.8-nm Emission Observed at Subauroral Latitudes Over 14 Years, Journal of Geophysical Research: Space Physics, 124, 9293–9301, https://doi.org/10.1029/2019JA026704, 2019.

Smalley, R. E., Wharton, L., and Levy, D. H.: The fluorescence excitation spectrum of rotationally cooled $NO_2$, The Journal of Chemical Physics, 63, 4977–4989, https://doi.org/10.1063/1.431244, 1975.

Spanswick, E., Liang, J., Houghton, J., Chaddock, D., Donovan, E., Gallardo-Lacourt, B., Keenan, C., Rosehart, J., Nishimura, Y., Hampton, D., and Gillies, M.: Association of structured continuum emission with dynamic aurora, Nature Communications, 15, https://doi.org/10.1038/s41467-024-55081-5, 2024.

Sternberg, J. R. and Ingham, M. F.: Observations of the Airglow Continuum, Monthly Notices of the Royal Astronomical Society, 159, 1–20, https://doi.org/10.1093/mnras/159.1.1, 1972.

SuperDARN Data Analysis Working Group. Participating Members, Thomas, E. G., Ponomarenko, P. V., Billett, D. D., Bland, E. C., Burrell, A. G., Kotyk, K., Reimer, A. S., Schmidt, M. T., Shepherd, S. G., Sterne, K. T., and Walach, M.-T.: SuperDARN Radar Software Toolkit (RST) 4.2, https://doi.org/10.5281/ZENODO.1403226, 2018.

SuperDARN Data Visualization Working Group, Martin, C., Rohel, R., Billett, D., Pitzer, P., Galeshuck, D., Kunduri, B., Khanal, K., Hiyadutuje, A., Chakraborty, S., Detwiller, M., and Schmidt, M.: SuperDARN/pydarn: pyDARN v4.1.2, https://doi.org/10.5281/ZENODO.3727269, 2025.

Syrjäsuo, M.: Software for Meridian Imaging Svalbard Spectrograph (MISS), https://github.com/UNISvalbard/KHO-MISS, 2025.

Tanskanen, E. I.: A comprehensive high-throughput analysis of substorms observed by IMAGE magnetometer network: Years 1993–2003 examined, Journal of Geophysical Research: Space Physics, 114, https://doi.org/10.1029/2008ja013682, 2009.

Tatum, J.: The interpretation of intensities in diatomic molecular spectra, Astrophysical Journal Supplement, 14, 21, 1967.

Vegard, L.: New types of emission spectra, Nature, 125, 14–14, 1930.

Wannberg, G., Wolf, I., Vanhainen, L. G., Koskenniemi, K., Röttger, J., Postila, M., Markkanen, J., Jacobsen, R., Stenberg, A., Larsen, R., Eliassen, S., Heck, S., and Huuskonen, A.: The EISCAT Svalbard radar: A case study in modern incoherent scatter radar system design, Radio Science, 32, 2283–2307, https://doi.org/10.1029/97RS01803, 1997.

Whiter, D. K., Lanchester, B. S., Gustavsson, B., Jallo, N. I. B., Jokiaho, O., Ivchenko, N., and Dahlgren, H.: Relative brightness of the $O^+(^2D–^2P)$ doublets in low energy aurorae, ApJ, 797, 64, https://doi.org/10.1088/0004-637X/797/1/64, 2014.

Yonker, J.: Spectroscopy of the $N_2$ Vegard-Kaplan bands in the dayglow, Ph.D. thesis, University of Alaska Fairbanks, http://hdl.handle.net/11122/6189, 2005.

Zhang, Y.-p., Deng, L.-h., Zhang, J., and Chen, Y.-q.: Rotational Analysis of $A^2\Pi_u–X^2\Sigma_g^+$ System of $^{14}N_2^+$, Chinese Journal of Chemical Physics, 28, 134–142, https://doi.org/10.1063/1674-0068/28/cjcp1410189, 2015.